Materials and Design 202 (2021) 109522

Contents lists available at ScienceDirect

Materials and Design

journal homepage: www.elsevier.com/locate/matdes

Multi-resonator metamaterials as multi-band metastructures

Vyacheslav Gorshkov [a,b], Pooya Sareh [c], Navid Navadeh [d], Vladimir Tereshchuk [a], Arash S. Fallah [d,e,f,*]

[a] Building 7, Department of Physics, National Technical University of Ukraine- Igor Sikorsky Kiev Polytechnic Institute, 37 Peremogy Avenue, Kiev-56 03056, Ukraine
[b] Theoretical Division, Los Alamos National Laboratory, Los Alamos, NM 87545, USA
[c] Creative Design Engineering Lab (Cdel), Department of Mechanical, Materials, and Aerospace Engineering, School of Engineering, University of Liverpool, Liverpool, The Quadrangle, Brownlow Hill L69 3GH, UK
[d] City and Guilds Building, Department of Aeronautics, South Kensington Campus, Imperial College London, London SW7 2AZ, UK
[e] Department of Machinery, Electronics and Chemistry, Oslo Metropolitan University, Pilestredet 35, 0166 Oslo, Norway
[f] ICP Institute of Computational Physics, ZHAW Zürich University of Applied Sciences, Wildbachstrasse 21, CH-8401 Winterthur, Switzerland

HIGHLIGHTS

- Multi-resonator acoustic metamaterials of BCC and FCC topologies are investigated.
- Physical origins of acoustic properties of such systems are expounded in detail.
- Simple formulae are proposed for prediction of passband boundary frequencies.
- Size and number of bandgaps are controlled through parameters of multivibrators.

GRAPHICAL ABSTRACT

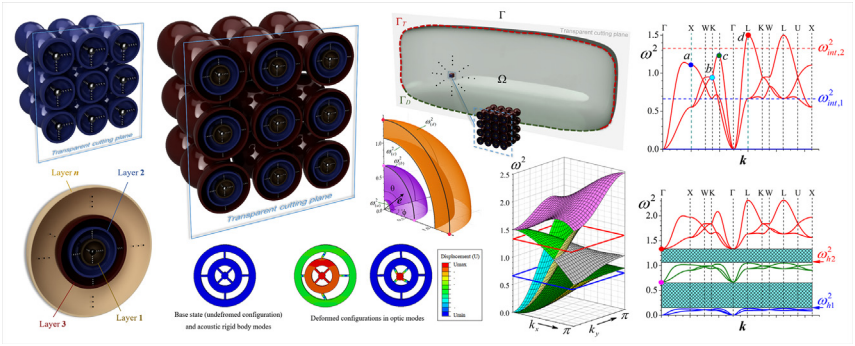

ARTICLE INFO

Article history:
Received 7 December 2020
Received in revised form 20 January 2021
Accepted 23 January 2021
Available online 27 January 2021

Keywords:
Multi-resonator
Phononic metamaterial
Acoustic mode
Optic mode
Bandgap
Dispersion surface

ABSTRACT

Introducing multi-resonator microstructure into phononic metamaterials provides more flexibility in bandgap manipulation. In this work, 3D-acoustic metamaterials of the body- and face-centered cubic lattice systems encompassing nodal isotropic multivibrators are investigated. Our main results are: (1) the number of bandgaps equals the number, n, of internal masses as each bandgap is a result of the classical analog of the quantum level-repulsion mechanism between internal and external oscillations, and (2) the upper boundary frequencies, $\omega^2_{upper^i}$, $i = 1, 2, \cdots, n$, of the gaps formed coincide with eigen-frequencies, $\omega^2_{int;i} \neq 0$, of the isolated multivibrator, $\omega_{upper^2;i} = \omega^2_{int;\,i}$, and the lower boundary frequencies, $\omega_{lower^2,i}{}^2$, are in good agreement with estimations as $\omega^2_{lower,i} \approx \widehat{\omega}^2_{int;i}$ $(\omega^2_{lower,i} < \widehat{\omega}^2_{int;i})$, where $\widehat{\omega}^2_{int;i}$ represent the eigen-frequencies of the multivibrator when its external shell is motionless.
The morphologies of the set of dispersion surfaces, $\omega^2_m(\boldsymbol{k})$, $m = 1, 2, \ldots, 6$, in the corresponding passbands are similar to each other and to that of the set of dispersion surfaces, $\omega^2_{ext;\,m}(\boldsymbol{k})$, obtained through the exclusion of internal masses. Thus, the problem of analyzing the acoustic properties of the complicated system is reduced to the study of two simple sets $\{\omega^2_{int;\,i}\}$ and $\left\{\widehat{\omega}^2_{int;i}\right\}$, along with $\{\omega^2_{ext;\,m}(\boldsymbol{k})\}$, the morphology of which depends only on the type of lattice symmetry. This splitting renders controlled phononic bandgaps formation in homogeneous multi-resonator metamaterials feasible.

* Corresponding author at: Department of Machinery, Electronics and Chemistry, Oslo Metropolitan University, Pilestredet 35, 0166 Oslo, Norway.
E-mail addresses: as3@imperial.ac.uk, arashsol@oslomet.no (A.S. Fallah).

https://doi.org/10.1016/j.matdes.2021.109522

1. Introduction

Phononic metamaterials, as synthesised latticed materials possessing microstructure, have been the subject of contemporary research due to their beneficial controllable features such as concurrent negative effective stiffness and density [1] and controllable frequency pass- and stop-bands [2]. These features, not observed in natural materials, render them useable in a variety of applications, including blast wave mitigation [3], seismic wave protection [4], enhanced flexural wave sensing [5], and several other applications where wave manipulation or guiding are relevant [6]. The microstructure in phononic metamaterials may comprise a single mass and spring (single resonator) or multiple masses and springs (multiple resonator) or such idealised realisations of other elements when feasible.

Introducing multiple resonators into the microstructure of phononic metamaterials adds new dimensions to bandgap formation, frequency spectral expansion, and passband expansion/contraction as a result of the additional degrees-of-freedom introduced [7,8]. Compared to their single resonator (SR) counterparts (Fig. 1(a)), multi-resonator (MR) metamaterials (Fig. 1(b)) possess more degrees-of-freedom per unit cell and, as a consequence, a higher number of dispersion surfaces and multiple bandgaps. SR metamaterials, such as those introduced by Lazarov and Janson [9] or Huang et al. [1], possess only a limited number of (in their case, two) complete bandgaps when acting as phononic filters rendering them unsuitable for some devices in need of multiple gaps. The solution is to increase the number of degrees-of-freedom in the microstructure through the introduction of additional elements. While several related ideas utilising more sophisticated microstructures such as fractals/pseudo-fractals [10], Labyrinthine acoustic metamaterials with space-coiling channels [11], and Hilbert curves [12] are proposed recently, extending the classic SR metamaterials using merely additional masses and springs proves to introduce distinctive features while the system's level of complexity remains undaunting.

The inclusion of microstructure also assists with narrowing down or extending the gap size through correct tuning of model parameters [2,13,14]. This is true of SR as well as MR metamaterials, however, MR metamaterials are more flexible due to an increased number of model parameters involved so the size of bandgaps may be appropriately tuned. It is therefore essential to investigate the primary features of MR metamaterials. While SR metamaterials of different topology and at several length scales are well studied (see e.g. [2,13,15–18]) there are a limited number of studies conducted on the characteristics of MR metamaterials (see e.g. [7,8,19–21]).

In the context of MR metamaterials, several forms are conceivable. While Huang and Sun [7] focused on the simple mass-spring-based design, Bonanomi et al. [22] discussed wave propagation in granular chains of directional filtering properties, Li [23] and Li et al. [24] came up with the design for acoustic diodes based on the hybrid tunable sonic crystal-multiphase gel units, Martinez-Sala et al. [25] investigated diffraction structures at macro length scales, and Gorishnyy et al. [26] proposed hypersonic phononic crystals. These studies are very interesting and form the basis of novel designs in the field [6], however, as mentioned before, we concentrate here on simple mass-spring models of MR with distinctive features.

Besides theoretical modelling, experimental research on the topic of design and testing phononic metamaterials has been ongoing ever since the conception of the idea, and some recent studies have focused on the topic. To mention but a few, Liu et al. [27] fabricated and tested sonic crystals encompassing localized resonant units and depicted spectral gaps with a lattice constant two orders of magnitude smaller than the relevant wavelength. They constructed and tested a 2 cm slab of the metamaterial which was shown to break the conventional mass-density law of sound transmission by one or more orders of magnitude at almost half a kilohertz. In another study conducted by Sheng et al. [28], a rigorous theoretical derivation of dynamic mass density yielded frequency-dependent values significantly deviating from the long-wavelength (static) value. The dynamic mass density was shown to be negative for certain frequency ranges (bandgaps) and the results were corroborated with experimental data. In a more recent study, Wang et al. [29] reported on the mechanism for simultaneous realization of perfect absorption and broadband insulation by layered acoustic metamaterials. They showed that at a particular frequency (312 Hz) nearly perfect absorption (98.4%) was achieved by testing a sample of 15 mm thickness. Barnhart et al. [19] conducted an experimental program to study dissipative MR metamaterials used for broadband elastic wave attenuation. This broadband wave attenuation was demonstrated through an impact test performed on finite samples where the frequency spectrum of the transmitted amplitude was found to be in

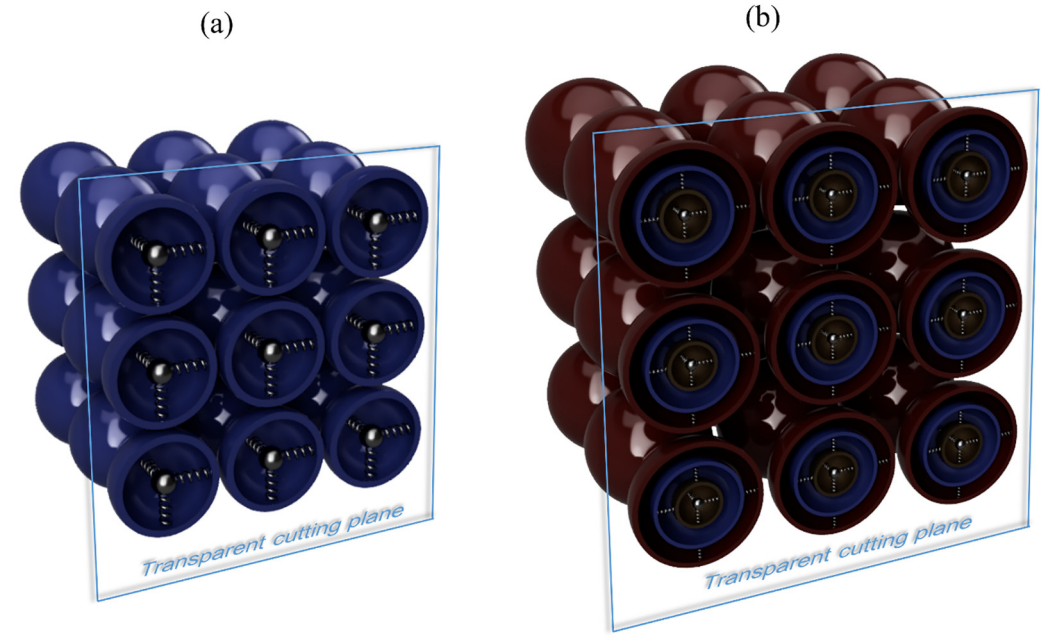

Fig. 1. Schematic of the microstructure in (a) single-resonator, and (b) multi-resonator phononic metamaterials.

close agreement with numerical results. Finally, in a rather recent study, Ma and Sheng [30] provided an overview of the topic as investigated over the one and half decades prior to their work.

Most results in this realm hinge upon the simple fact that composites with locally resonant microstructure within their unit cells exhibit simultaneous negative effective density and stiffness at certain frequency ranges. While the experimental study of this class of metamaterials is interesting in itself and essential to adduce evidence in support of the theoretical results obtained also to depict the physical significance of parameters defining the models investigated, such a study falls beyond the scope of the present paper as it merits a great deal of research on its own.

This paper is organised in 5 sections as follows: following this introduction, the discrete-parameter multi-resonator metamaterial is formulated in Section 2. Each MR unit comprises mass points of zero rotatory inertia and is connected to adjacent masses by massless linear springs of equal stiffness in each direction (local isotropy). The two kinds of connectivity of MR units considered are those of the BCC and FCC structures. In Section 3, the BCC MR metastructure is analyzed and its results expounded. In Section 4, the FCC lattice is considered. In each case, dispersion surfaces are tuned to form bandgaps and passbands. Finally, the study is concluded in Section 5.

2. Analyses

2.1. The discrete-parameter multi-resonator (MR) metamaterial

The discrete-parameter MR metamaterial is an idealisation of scenarios where mass and springs stand for structural elements, as in Fig. 2(a). When MR units are embedded in a continuum, as if connected by external springs in a given topology, the MR metamaterial is ensued (See Fig. 2(b)). When feasible assumptions are made regarding the distribution of mass and stiffness in the system, the discrete-parameter model is resulted in and the equations of motion may be cast in a simple form. Considering a three-dimensional metamaterial comprising an infinite arrangement of locally resonant mass-spring MR's connected in a given topology, as shown schematically in Fig. 2(b), the equations of motion for different layers of the mass-spring model (Fig. 2(a)) are derived as follows:

$$m_1\ddot{q}_1 + k_1^q(q_1 - q_2) = 0 \quad \text{for the innermost layer} \tag{1}$$

$$m_p\ddot{q}_p + \left(k_p^q + k_{p-1}^q\right)q_p - k_p^q q_{p+1} - k_{p-1}^q q_{p-1} = 0 \quad \text{for intermediate layers } (1 < p < n) \tag{2}$$

where the layers are numbered from inside outwards; m_p is the mass of layer p; and k_p^q is the stiffness of the spring connecting layer p to layer $p+1$ in the direction of q, where q designates a generalized coordinate which may be the x, y, or z components of the displacement vector in the cartesian coordinate system. Equations of motion for the outermost layer depend upon the external topology of MR units in the metamaterial and may be complicated, in general. In this work, two different well-known topologies of the BCC and FCC lattices are considered which render local interactions of each MR unit with immediately adjacent ones possible. In the sequel, the equations of motion are derived for both topologies and subsequent analyses performed which make it possible to derive the dispersion surfaces and bandgap structures for each case, corresponding to acoustic and optic modes of vibration (Fig. 2(c)).

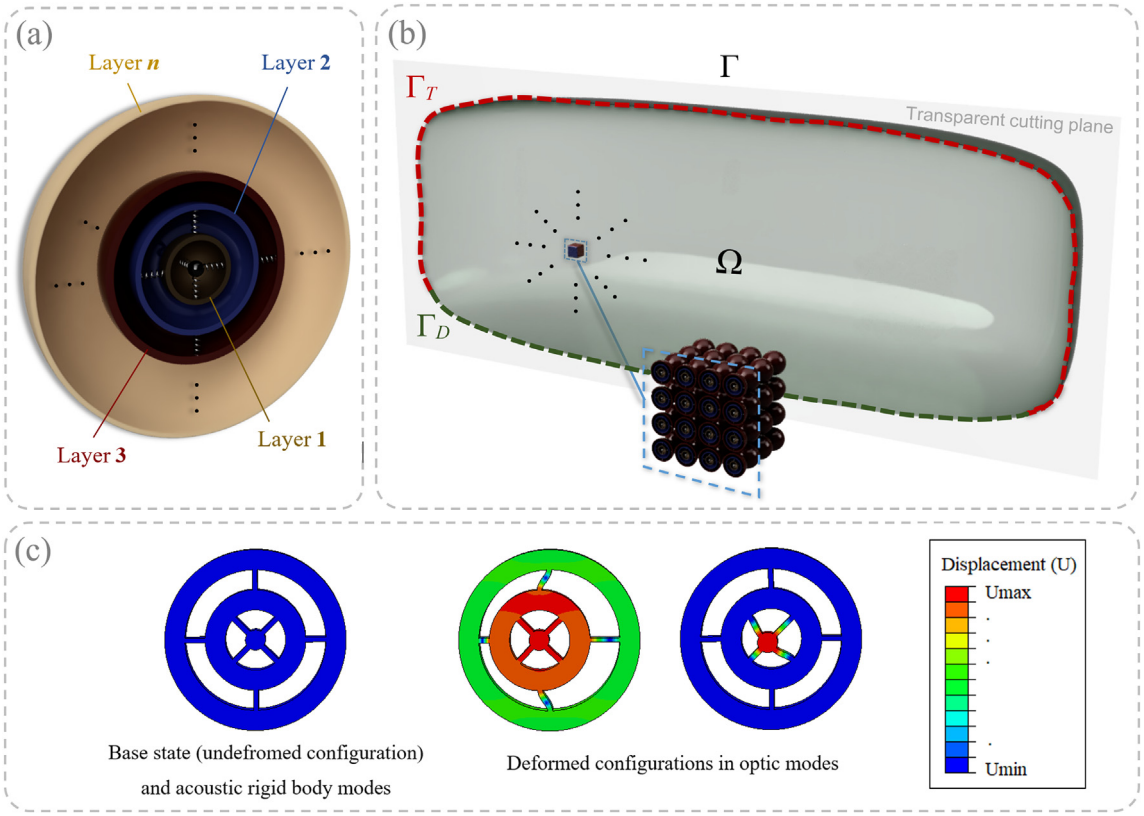

Fig. 2. (a) Schematic of an N-layered mass-in-mass unit in an MR metamaterial. (b) A medium with multi-resonator microstructure (external connections may be defined using spring elements). (c) The schematic of a scenario when MR ($n = 3$) mass-spring idealisation is possible. The base state (undeformed configuration) and acoustic rigid body modes, as well as deformed configurations in optic modes, are distinguishable.

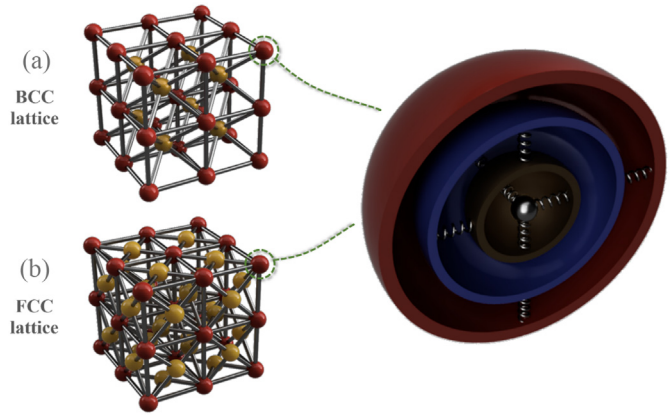

Fig. 3. External topologies of the MR units in the (a) BCC, and (b) FCC lattices.

2.2. Analysis of the MR metamaterial

As mentioned before, two topologies, namely the BCC and FCC, are considered here to represent the external connectivity of the MR units. The BCC and FCC topologies are selected as they replicate two of the topologies encountered in nature, for instance in crystalline metals. Fig. 3 shows both of these topologies in 3D along with the nodal microstructure for a four-layered resonator, as an example.

3. The BCC-multi-resonator mass-in-mass structure

3.1. Formulation of the problem

The dispersion equation for the BCC structure under consideration is based on two basic relations. If two locally resonant elements of the system are connected by a spring of stiffness κ, then the second element acts on the first one with a force, $\boldsymbol{f}_{12}$ of Eq. (3).

$$\boldsymbol{f}_{12} = \kappa \boldsymbol{e}_{12}[\boldsymbol{e}_{12}.(\boldsymbol{x}_2 - \boldsymbol{x}_1)] \tag{3}$$

Here $\boldsymbol{x}_1$ and $\boldsymbol{x}_2$ are the displacements of the spring ends from the equilibrium position, $\boldsymbol{e}_{12}$ – the unit vector directed along the spring, and the displacements are assumed to be small i.e. $|\boldsymbol{x}_2 - \boldsymbol{x}_1| \ll l$, where l is the unstretched length of the spring.

When a wave propagates in an infinite medium, the displacements, $\boldsymbol{x}_1$, $\boldsymbol{x}_2$, in the equivalent nodes of the structure with coordinates, $\boldsymbol{r}_1$, $\boldsymbol{r}_2$, are related by Bloch's equation as follows:

$$\boldsymbol{x}_2 = \boldsymbol{x}_1 e^{i\,(\boldsymbol{r}_2 - \boldsymbol{r}_1)\boldsymbol{k}} \tag{4}$$

where $\boldsymbol{k}$ is the wave vector, and the vector $\boldsymbol{r}_2 - \boldsymbol{r}_1$ is a translational symmetry vector.

The unit cell of the BCC structure includes two lattice nodes (Fig. 4) and the corresponding lattice constant is equal to a. Blue and red nodes form simple cubic lattices which are then inserted into each other to create the model. Nodes A and B (marked with circles) are used as 'reference nodes'. As such, the displacement of any other structural node is associated with the displacement of the corresponding reference node through Eq. (4). For the selected shape of the unit cell (instead of a truncated octahedron, which contains one node only), the Brillouin zone in $\boldsymbol{k}$-space is a cube of side length $2\pi/a$.

As an infinite lattice with this unit cell, the dynamics of the entire system can be described by equations for the displacements of the reference nodes represented by a column vector, $\boldsymbol{X}$, composed of 18 entries as in Eq. (5).

$$\boldsymbol{X} = \begin{bmatrix} \boldsymbol{X}_{ext} \\ \boldsymbol{X}_{int} \\ \boldsymbol{X}_{nuc} \end{bmatrix}, \boldsymbol{X}_{ext} = \begin{bmatrix} x_a \\ y_a \\ z_a \\ x_b \\ y_b \\ z_b \end{bmatrix}, \boldsymbol{X}_{int} = \begin{bmatrix} x_{ai} \\ y_{ai} \\ z_{ai} \\ x_{bi} \\ y_{bi} \\ z_{bi} \end{bmatrix}, \boldsymbol{X}_{nuc} = \begin{bmatrix} x_{an} \\ y_{an} \\ z_{an} \\ x_{bn} \\ y_{bn} \\ z_{bn} \end{bmatrix} \tag{5}$$

In relations (5), $\boldsymbol{X}_{ext}$ represents the displacement vectors of the outer shells for the reference nodes A and B of mass M (see Fig. 4), $\boldsymbol{X}_{int}$ are the displacements of the inner shells of mass m_i, and $\boldsymbol{X}_{nuc}$ are the displacements of the inner cores in nodes A and B (the mass of the core is m_n). As mentioned before, nodes A and B have an identical internal structure (local homogeneity) (the stiffness of internal springs is indicated in Fig. 4). The stiffness of external springs connecting the nodes of the same sublattice is χ (in Fig. 4(a), for example, these are the springs between the neighboring blue nodes). The stiffness of springs that connect

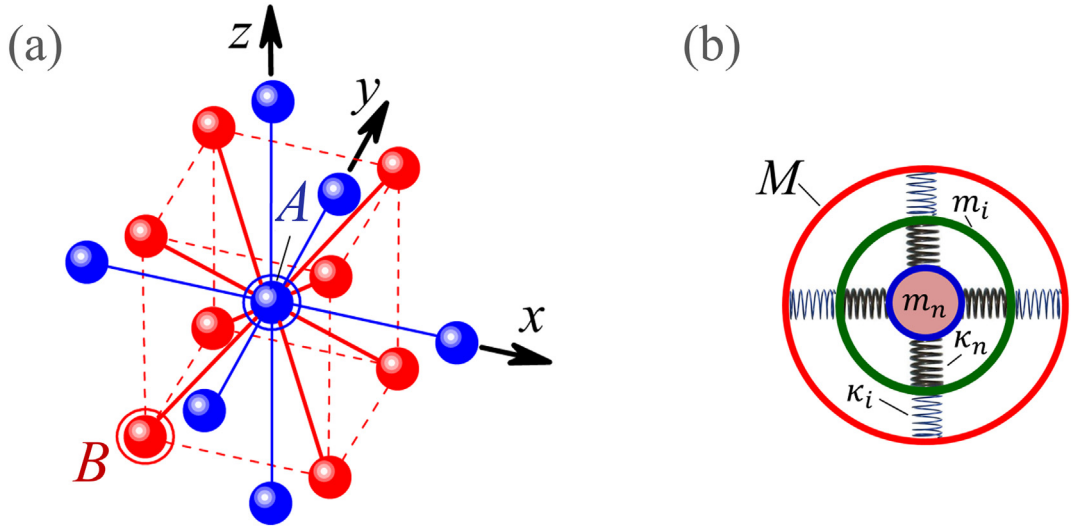

Fig. 4. (a) The unit cell of the BCC structure (confined by red dashed lines) and the schematic of external elastic bonds between its nodes. Blue and red spheres represent two simple cubic lattices inserted into each other. (b) The internal structure of nodes (A and B). The inner shells/cores are connected to the corresponding outer shells by six springs, each of which is perpendicular to four adjacent springs. The stiffness of the springs and the masses of the inner shells and cores are indicated in the figure. (For interpretation of the references to colour in this figure legend, the reader is referred to the web version of this article.)

adjacent nodes belonging to different sublattices is derived as $\varkappa = 2\chi/\sqrt{3}$, provided that the stiffness of each spring is inversely proportional to its length, i.e.:

$$\chi \sim 1/a, \varkappa \sim 1/\left(a\sqrt{3}/2\right), \chi/\varkappa = \sqrt{3}/2 \tag{6}$$

Now, we derive the equations of motion for only the outer shells of reference nodes, i.e. without taking into account their internal microstructure. To this end, we take into consideration all the forces, caused by 6 neighboring blue nodes (see Fig. 4(a)) and 8 red nodes, acting on the reference node *A*. Similar calculations are performed for reference node *B*. The basis of these calculations is presented in Eqs. (3) and (4). For example, when calculating the forces exerted by 8 neighboring red nodes and acting on the reference node *A*, it should be taken into account that their displacements are related by the equation:

$$\boldsymbol{X}_j^{(red)} = \boldsymbol{X}_B^{(red)} e^{\left[i\boldsymbol{k}a\left(\boldsymbol{e}_{BA}+\boldsymbol{e}_j\right)/2\right]} \tag{7}$$

Here $\boldsymbol{e}_{BA}$ is the vector directed from the reference node *B* to the reference node *A*, $\boldsymbol{e}_j$ is the unit vector directed from the reference node *A* to one of the neighboring red nodes ($j = 1, 2, 3, \ldots, 8$), and $\boldsymbol{X}_B^{(red)}$ is the displacement of the reference node *B*. As a result, we obtain the following system of equations:

$$M\ddot{\boldsymbol{X}}_{ext} = \begin{bmatrix} \boldsymbol{A} & \boldsymbol{B} \\ \boldsymbol{B}^* & \boldsymbol{A} \end{bmatrix} \cdot \boldsymbol{X}_{ext} \equiv \boldsymbol{F}_{\boldsymbol{ext}} \cdot \boldsymbol{X}_{ext} \tag{8}$$

The third-order matrix, $\boldsymbol{A}$, describes the interaction of nodes in each of the blue and red sublattices while the matrices $\boldsymbol{B}$ and $\boldsymbol{B}^*$ (complex conjugate of $\boldsymbol{B}$) represent the mutual influence of the sublattices on one another.

$$\mathbf{A} = 2\chi \cdot \boldsymbol{A\prime} - \frac{8\varkappa}{3} \cdot \boldsymbol{I_3} \tag{9}$$

$$\boldsymbol{A\prime} = \begin{bmatrix} \cos(k_x)-1 & 0 & 0 \\ 0 & \cos(k_y)-1 & 0 \\ 0 & 0 & \cos(k_z)-1 \end{bmatrix} \tag{10}$$

Hereinafter, by the wave vector, $\boldsymbol{k}$, we mean the dimensionless wave vector, i.e. $|\boldsymbol{k}|a = \frac{2\pi a}{\lambda} = k$, where λ is the wavelength, $\boldsymbol{I}_n$ is the identity matrix of the *n*-th order, and the following relations hold:

$$\boldsymbol{B} = \xi \cdot \boldsymbol{B}' \tag{11}$$

$$\boldsymbol{B}' = \begin{bmatrix} \alpha_1+\alpha_2+\alpha_3+\alpha_4 & \alpha_1-\alpha_2+\alpha_3-\alpha_4 & \alpha_1-\alpha_2-\alpha_3+\alpha_4 \\ \alpha_1-\alpha_2+\alpha_3-\alpha_4 & \alpha_1+\alpha_2+\alpha_3+\alpha_4 & \alpha_1+\alpha_2-\alpha_3-\alpha_4 \\ \alpha_1-\alpha_2-\alpha_3+\alpha_4 & \alpha_1+\alpha_2-\alpha_3-\alpha_4 & \alpha_1+\alpha_2+\alpha_3+\alpha_4 \end{bmatrix} \tag{12}$$

$$\xi = \frac{2}{3}\varkappa e^{\left[i\left(k_x+k_y+k_z\right)/2\right)]}, \text{and } \varkappa = 2\chi/\sqrt{3} \tag{13}$$

where α_i are the functions of wave vector components and related to them as follows:

$$\begin{aligned} \alpha_1 &= \cos\left[\frac{k_x+k_y+k_z}{2}\right], \alpha_2 = \cos\left[\frac{-k_x+k_y+k_z}{2}\right] \\ \alpha_3 &= \cos\left[\frac{-k_x-k_y+k_z}{2}\right], \text{and } \alpha_4 = \cos\left[\frac{k_x-k_y+k_z}{2}\right] \end{aligned} \tag{14}$$

When we take into account the fact that the lattice nodes have an internal microstructure, we obtain a system of equations as:

$$\begin{bmatrix} M\cdot\ddot{\boldsymbol{X}}_{ext} \\ m_i\cdot\ddot{\boldsymbol{X}}_{int} \\ m_n\cdot\boldsymbol{X}_{nuc} \end{bmatrix} = \begin{bmatrix} \boldsymbol{F}_{ext}-2\kappa_i\cdot\boldsymbol{I}_6 & 2\kappa_i\cdot\boldsymbol{I}_6 & 0 \\ 2\kappa_i\cdot\boldsymbol{I}_6 & -(2\kappa_i+2\kappa_n)\cdot\boldsymbol{I}_6 & 2\kappa_n\cdot\boldsymbol{I}_6 \\ 0 & 2\kappa_n\cdot\boldsymbol{I}_6 & -2\kappa_n\cdot\boldsymbol{I}_6 \end{bmatrix} \cdot \begin{bmatrix} \boldsymbol{X}_{ext} \\ \boldsymbol{X}_{int} \\ \boldsymbol{X}_{nuc} \end{bmatrix} \tag{15}$$

In the sequel, for a qualitative analysis of acoustic properties of the system under consideration, it is useful to know the eigenfrequencies of the isolated lattice nodes i.e. without taking into consideration the influence of external springs. These can be found from the truncated system of Eq. (15) if we single out the equations of motion for the displacements of the outer shell of the node, x_e, its inner shell, x_i, and its core, x_n, at $\chi = 0$ as in Eq. (16).

$$\begin{bmatrix} M\cdot\ddot{x}_e \\ m_i\cdot\ddot{x}_i \\ m_n\cdot\ddot{x}_n \end{bmatrix} = -\begin{bmatrix} 2\kappa_i & -2\kappa_i & 0 \\ -2\kappa_i & 2\kappa_i+2\kappa_n & -2\kappa_n \\ 0 & -2\kappa_n & 2\kappa_n \end{bmatrix} \cdot \begin{bmatrix} x_e \\ x_i \\ x_n \end{bmatrix} \tag{16}$$

In the model chosen, it suffices to consider the one-dimensional problem as the excited internal oscillations are independent (due to the geometric linearity approximation) along arbitrarily defined perpendicular directions. For the periodic solutions, i.e. $x = x_0 \exp(i\omega t)$, there are two non-zero eigenfrequencies (the third solution of Eq. (15), $\omega^2 = 0$ corresponds to the free movement of the node as a whole):

$$\omega_{int;1,2}^2 = \frac{1}{2}\left[\omega_i^2+\omega_n^2 \pm \sqrt{\left(\omega_i^2-\omega_n^2\right)^2+4\omega_{in}^4}\right] \tag{17}$$

where.

$$\omega_0^2 \equiv \omega_i^2 = \frac{2\kappa_i}{\mu_{ei}}, \mu_{ei} = \frac{Mm_i}{M+m_i} \tag{18}$$

$$\omega_n^2 = \frac{2\kappa_n}{\mu_{in}}, \mu_{in} = \frac{m_i m_n}{m_i+m_n} \tag{19}$$

$$\omega_{in}^4 = 4\frac{\kappa_i\kappa_n}{m_i^2} \tag{20}$$

The frequency $\omega_0^2 \equiv \omega_i^2$ represents the eigenfrequency of an isolated node in the absence of a core, while the frequency ω_n^2 corresponds to the natural oscillations of the isolated inner shell-core pair.

The equation for the eigenfrequencies and eigenvectors characterizing the acoustic properties of the entire system is obtained based on Eq. (15), represented in the form $\boldsymbol{X} = \boldsymbol{X}_0 \exp(i\omega t)$ thus:

$$-\omega^2\boldsymbol{X_0} = \begin{bmatrix} \boldsymbol{F}_{ext}-\frac{\gamma}{1+\gamma}\cdot\boldsymbol{I_6} & \frac{\gamma}{1+\gamma}\cdot\boldsymbol{I_6} & \boldsymbol{0} \\ \frac{1}{1+\gamma}\cdot\boldsymbol{I_6} & -\frac{\gamma+\beta}{1+\gamma}\cdot\boldsymbol{I_6} & \frac{\beta}{1+\gamma}\cdot\boldsymbol{I_6} \\ \boldsymbol{0} & \frac{\alpha\beta}{1+\gamma}\cdot\boldsymbol{I_6} & -\frac{\alpha\beta}{1+\gamma}\cdot\boldsymbol{I_6} \end{bmatrix} \cdot \boldsymbol{X_0} \tag{21}$$

In Eq. (21), the frequency ω is given in units of ω_0 where:

$$\widetilde{\boldsymbol{F}}_{\boldsymbol{ext}} \equiv \begin{bmatrix} \widetilde{\boldsymbol{A}} & \widetilde{\boldsymbol{B}} \\ \widetilde{\boldsymbol{B}}^* & \widetilde{\boldsymbol{A}} \end{bmatrix} \tag{22}$$

$$\widetilde{\boldsymbol{A}} = \Omega^2 \cdot \frac{3\sqrt{3}}{16} \cdot \boldsymbol{A}' - \frac{\Omega^2}{2} \cdot \boldsymbol{I}_3, \widetilde{\boldsymbol{B}} = \Omega^2 \cdot \frac{1}{8} \cdot \boldsymbol{B}' \tag{23}$$

$$\gamma = \frac{m_i}{M}, \alpha = \frac{m_i}{m_n}, \beta = \frac{k_n}{k_i}, \text{and } \Omega^2 = \frac{16}{3\sqrt{3}}\left(\frac{2\chi}{M}\right)/\omega_0^2 \tag{24}$$

Since the matrix of the system of equations in Eq. (21) is a function of the wave vector $\boldsymbol{k}$, Eq. (20) defines, in the general case, 18 dispersion-surfaces $\omega(\boldsymbol{k})$ in the four-dimensional (4D) space. Four parameters, α,

β, γ, and Ω^2 - which determine the acoustic properties of the system - have a transparent physical sense (including Ω^2 - see the next section) and are easily controlled.

3.2. Acoustic properties of the system

The presence of multivibrators inside the lattice nodes leads to the formation of both separate passband regions and bandgaps in the frequency spectrum. Below, we show that the corresponding boundary frequencies can be established as the simple mathematical relations of a clear qualitative interpretation.

We demonstrate the indicated acoustic properties of the system using the results obtained for a specific set of parameters (Figs. 5 and 8: $\alpha = 2, \beta = 1, \gamma = 2$, and $\Omega^2 = 1.5$). Note that the parameter Ω^2 (see Eq. (24) and Fig. 5) corresponds to the frequency of lattice vibrations at $\boldsymbol{k} = \boldsymbol{0}$ in the case when internal multivibrators are removed from the system. Such (thrice degenerate) vibrations (according to the shape of the Brillouin zone for the selected unit cell) are equivalent to vibrations with the wave vector $k_{x,\,y,\,z} = 2\pi$ and wavelength $\lambda = 1$ (in the units of the lattice constant a). In other words, each of the sublattices of the system is shifted, as a whole, relative to the other sublattice along one of the coordinate axes x, y, or z. In this case, the neighboring planes of lattice sites with an orientation of the type [100] are displaced in the antiphase without deformation of the springs in the sublattices.

Oscillations at the boundary point $\boldsymbol{k}(\pi,\pi,0)$ in Fig. 5 (point $M_{1,\,2}$ in Fig. 12) also correspond to antiphase displacements of neighboring planes of nodes ([110] -type) with frequencies:

$$\omega^2_{M,1} = \frac{4}{3\sqrt{3}}\left(\frac{4\chi}{M}\right)/\omega_0^2, \omega^2_{M,2} = \left(\frac{4\chi}{M}\right)/\omega_0^2, \text{and}$$
$$\omega^2_{M,3} = \frac{4\chi}{M}\left(1+\frac{8}{3\sqrt{3}}\right)/\omega_0^2 \approx 1.65 \times \Omega^2 \quad (25)$$

The first two frequencies correspond to transverse vibrations, and the third to longitudinal. For future estimates, we note that $\omega^2_{M,\,3}$ is the maximum frequency in the first Brillouin zone. This follows from the truncated system of Eq. (21), if we exclude from consideration internal multivibrators:

$$-\omega^2 \boldsymbol{X}_{ext} = \left[\widetilde{\boldsymbol{F}}_{ext}\right]\cdot\boldsymbol{X}_{ext}, \left|\widetilde{\boldsymbol{F}}_{ext}(\boldsymbol{k}) + \omega^2\cdot\boldsymbol{I}_6\right| = 0 \quad (26)$$

For individual values of the wave vector, $\boldsymbol{k}$, the dispersion equation (Eq. (26)) can be easily solved analytically. At the point $\boldsymbol{k}(\pi,\pi,\pi)$ (point R in Fig. 12), the longitudinal and transverse vibrations have the same frequency $\omega^2_R = \frac{4\chi}{M}\left(1+\frac{4}{3\sqrt{3}}\right)/\omega_0^2$; point $\boldsymbol{k}(\pi,0,0)$ (point X in Fig. 12) corresponds to twice degenerate transversal oscillations with frequency $\omega^2_{X1,2} = \frac{4}{3\sqrt{3}}\left(\frac{4\chi}{M}\right)/\omega_0^2$ and longitudinal oscillations with frequency $\omega^2_{X,3} = \frac{4\chi}{M}\left(1+\frac{4}{3\sqrt{3}}\right)/\omega_0^2$.

The planes outlined in Fig. 5(a) with red and blue contours are corresponding to surfaces:

$$\omega^2 = \omega^2_{int;1,2} \quad (27)$$

where $\omega^2_{int;\,1,\,2}$ are the eigenfrequencies of isolated nodes (see Eq. (15)). When defined in terms of dimensionless parameters these are recast as:

$$\omega^2_{int;1,2} = \frac{1}{2}\left[1+\beta\left(\frac{1+\alpha}{1+\gamma}\right) \pm \sqrt{\left(1-\beta\left(\frac{1+\alpha}{1+\gamma}\right)\right)^2 + 4\frac{\beta}{(1+\gamma)^2}}\right] \quad (28)$$

For the parameters given above $\omega^2_{int;\,1} = 2/3$, $\omega^2_{int;\,2} = 4/3$.

The result of the interaction between external and internal elastic forces is shown in Fig. 6(a). The brief qualitative interpretation of this is quite transparent. The internal structure of lattice nodes defines the isotropy of their elastic properties. In this case, a coupling strength between external and internal vibrational modes manifests itself

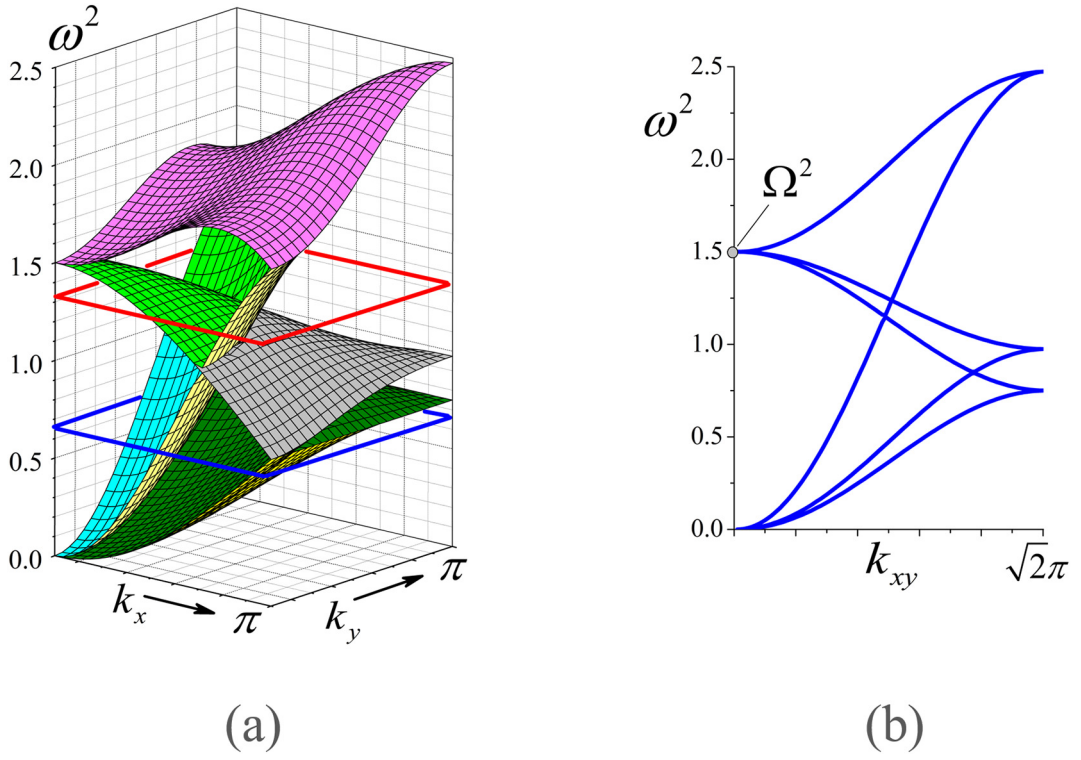

Fig. 5. (a) Dispersion surfaces calculated for lattice vibrations without taking into account the internal structure of nodes ($\Omega^2 = 1.5$). The wave vector k changes in the first quadrant of the plane (k_x,k_y), and $k_z = 0$. (b) Cross-section of the surfaces presented in part (a): $k_x = k_y \equiv k_{xy}/\sqrt{2}$.

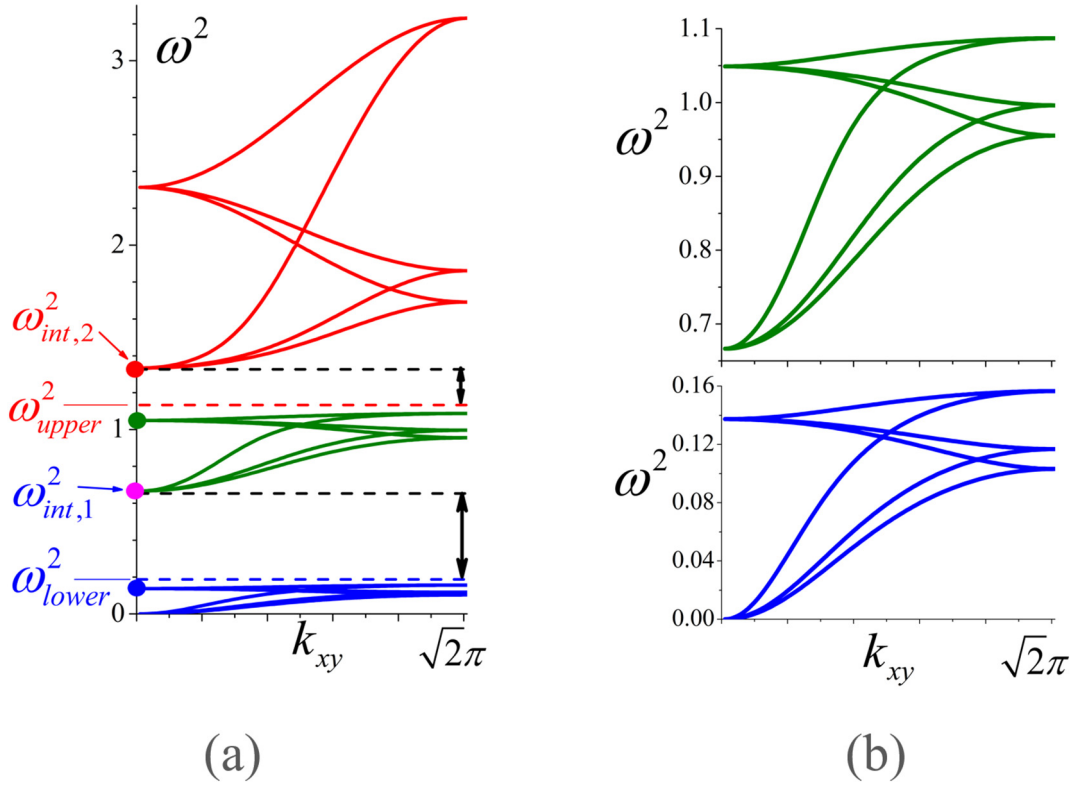

Fig. 6. (a) Cross-sections of frequency surfaces ($k_x = k_y \equiv k_{xy}/\sqrt{2}, k_z = 0$), taking into account the internal structure of the lattice nodes. $\Omega^2 = 1.5$, $\alpha = 2$, $\beta = 1$, and $\gamma = 2$. (b) A more detailed representation of the blue and olive dependencies given in part (a). (For interpretation of the references to colour in this figure legend, the reader is referred to the web version of this article.)

through the influence of external/internal elastic forces on the outer shells. At the lines of intersection of the planes $\omega^2 = \omega^2_{int;\,1,\,2}$ (see Eq. 28) and surfaces $\omega^2 = \omega^2(\boldsymbol{k})$ (see Fig. 5(a)) these modes have the same frequency and the same polarization, so that effects analogous to the quantum effect of energy-level repulsion arise (see [27]):

$$M\ddot{x_e} = -(\chi + k_i)x_e + k_i x_i = -\omega^2 M x_e \text{ and } m\ddot{x_i} = k_i x_e - k_i x_i = -\omega^2 m x_i \tag{29}$$

the surfaces $\omega^2 = \omega^2(\boldsymbol{k})$ are essentially 'torn up' by planes $\omega^2 = \omega^2_{int;\,1,2}$. The reconnection of these 'primary' dispersion surfaces is followed by the formation of bandgaps (see Fig. 6(a)). On the adjacent newly formed upper frequency surfaces ($\omega^2(\boldsymbol{k})$ is higher than the corresponding value $\omega^2_{int;\,i}$), the external elastic forces act on the outer shells antiphase with internal forces. On the lower adjacent surfaces ($\omega^2(\boldsymbol{k}) < \omega^2_{int;\,i}$) these forces act in phase. Thus, the maximal frequency on these surfaces can be achieved when the result of the 'in-phase displacements' vanishes, in other words, the outer shells are stationary. The analogs of the bandgap/passband formation mechanism discussed manifest themselves in other physical systems. The passband for electromagnetic (EM) waves in metals corresponds to the frequencies, ω_{EM}, that is higher than the eigenfrequency of plasma oscillations, ω_{plasma}, in the system of electrons and positive charged nuclei. More complex examples of the formation of passbands/bandgaps were realized by the interaction of EM waves with saturated atomic cesium vapor as shown in previous studies [31].

It is important to establish the quantitative characteristics of the passband regions (alternatively bandgaps) as a function of parameters defining the acoustic system. To this end, we consider a simpler problem when the internal structure of the node is represented by a simple vibrator (see the inset in Fig. 8). Examples of its solution, by analogy with the results of Figs. 5 and 6 are shown in Fig. 7. We draw attention to the fact that the topology of dependencies $\omega^2(k_{xy})$ in each passband region, shown in Fig. 6 and Fig. 7(c) and (d), is similar to the structure of the frequency dependencies of the system in the "initial" (without internal structure) state - see Fig. 5 and Fig. 7(a) and (b). Let us consider, in detail, factors determining the result of splitting of this initial state into separate zones.

The interaction between external and internal elastic media does not depend on the nature of the external elastic forces that cause vibrations of the node shell (see the inset in Fig. 8) with a certain angular frequency, $\sqrt{\chi/M}$, at $m_i = 0$. Taking into account the internal structure of the node leads to the formation of hybrid frequencies, which are easy to determine from the system of equations of motion for the displacements of the outer shell, x_e, and internal mass, x_i.

The corresponding dimensionless hybrid frequencies are equal to:

$$\omega^2_{h1,2} = \frac{1}{2}\left(\Omega_e^2 + 1 \pm \sqrt{\left(\Omega_e^2 + 1\right)^2 - 4\Omega_e^2/(1+\gamma)}\right) \tag{30}$$

where $\Omega_e^2 = (\chi/M)/\omega_0^2, \omega_0^2 = k_i/\mu, \mu = Mm/(M+m)$, and $\gamma = m/M$. (The dimensionless eigenfrequency of an isolated node, ω_0^2, in Fig. 8 is equal to 1). The main result of the solution of the problem is that the lower hybrid frequency has an upper limit (see Fig. 8):

$$\lim_{\Omega^2 \to \infty} \omega_1^2 = 1/(1+\gamma) < \omega_0^2 \equiv 1 \tag{31}$$

The limit value $1/(1+\gamma)$ can be obtained from qualitative considerations that lead to a simple method for calculating hybrid frequencies for a multi-level internal structure of nodes.

In the case of free vibrations of an isolated node, the displacements of the shell and the core are out of phase and the displacement of the system's centre of mass is identically zero - $Mx_e(t) + mx_i(t) = 0$. The

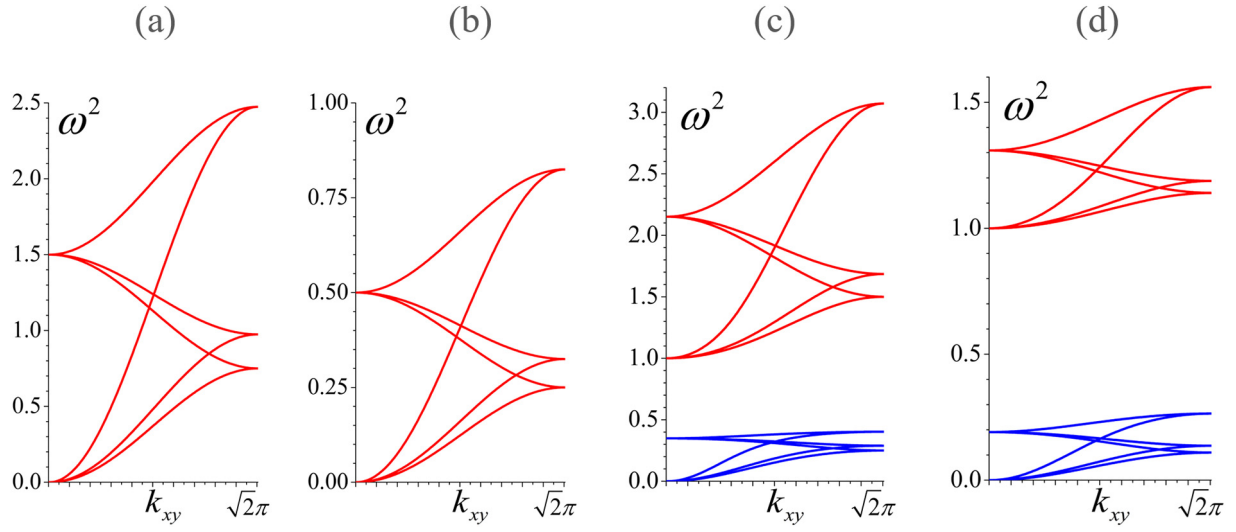

Fig. 7. (a) and (b): Initial (without internal structure) set of dependences $\omega^2(k)$. (a): $\Omega^2 = 1.5$ and $\gamma = 1$; (b) $\Omega^2 = 0.5$ and $\gamma = 1$. (c) and (d): Effects of manifestation of the internal structure of nodes in variants *A* and *B*, respectively. In the center of the Brillouin zone, the optical branches of the oscillations are derived from the eigenfrequency of the vibrator ($\omega^2(k = 0) = 1$) and two hybrid frequencies 2.15 and 0.35 (c), and 1.31 and 0.19 (d).

influence of an external field changes the frequency of internal oscillations and shifts the center of mass of the node with time. However, these forced vibrations can be represented as free vibrations of an isolated node with the effective mass of the outer shell $M^* = -mx_i(t)/x_e(t)$, which ensures the immobility of the center of mass of the node. At the lower hybrid frequency, the displacements $x_i(t)$ and $x_e(t)$ are in phase and $M^* < 0$. On the other hand, the eigenfrequency of oscillations of the node is $\omega_h^2 = \frac{k_i}{\mu} = \left(\frac{k_i}{m}\right)\left(1 + \frac{m}{M^*}\right)$. As the stiffness of the external spring increases, the displacement value $x_e(t) \to 0$, and the effective mass $M^* \to -\infty$, thereby bringing the value of ω_h^2 to the upper limit $\left(\frac{k_i}{m}\right)$. Its dimensionless quantity, $\left(\frac{k_i}{m}\right)/\omega_0^2$, is equal to the value of $1/(1+\gamma)$ obtained from Eq. (31), and represents the eigenfrequency of internal vibrations under the assumption that the outer shell of the node is motionless.

The analysis of the results presented in Fig. 7 leads to the following assumption. The presence of an internal vibrator splits each function, $\omega^2 = \omega^2(\boldsymbol{k})$, presented in Fig. 7(a) and (b), into two hybrid dependences, $\omega_{h1}^2[\omega^2(\boldsymbol{k})]$, $\omega_{h,2}^2[\omega^2(\boldsymbol{k})]$, in accordance with Eq. (28), in which $\Omega_e^2 \equiv \omega^2(\boldsymbol{k})$. Two passband regions are formed - upper and lower (see Fig. 7(c–d)). In particular, the point $\Omega_e^2 = 0$ gives rise to the lower ($\omega^2(\boldsymbol{k} = \boldsymbol{0}) = 0$) and upper passband regions, $\omega^2(\boldsymbol{k} = \boldsymbol{0}) = 1$ (recall that this frequency coincides with the eigenfrequency of the internal vibrations of an isolated node). The formation of the bandgap occurs because the lower hybrid frequency is bounded from above (see Fig. 8).

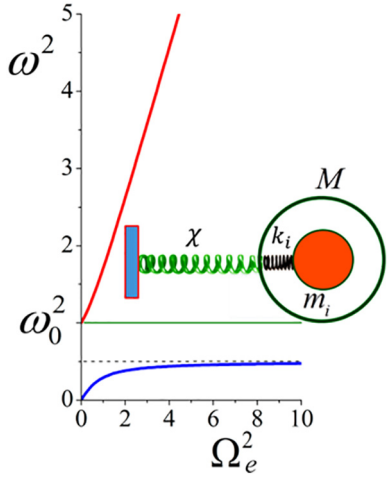

Fig. 8. Solutions of Eq. (30) and the scheme of the object under consideration.

The result obtained can be generalized to the case of a multilevel metastructure of $\backslash-1$ internal multivibrators possessing $\backslash-1$ internal elements/masses (Fig. 2(a)). The total number, $\backslash$, of elements of an isolated node determine its $\backslash$ eigenfrequencies as: $\omega_{int,0}^2 = 0, \omega_{int,1}^2, \omega_{int,2}^2, \ldots..,$ $\omega_{int,\backslash-1}^2$, which subsequently represent the lower boundaries of the passband regions. The upper boundaries of these regions (or the lower boundaries of the bandgaps) are guaranteed to represent eigenfrequencies: $\omega_{h,1}^2, \omega_{h,2}^2, \omega_{h,3}^2, \ldots.., \omega_{h,\backslash-1}^2$ of an isolated node under the assumption that its outer shell is motionless. Bandgaps thus correspond to frequency intervals:

$$\Delta_{sup,i}^{(\omega^2)} = \omega_{int,i}^2 - \omega_{h,i}^2, i = 1, 2, \ldots, \backslash-1 \tag{32}$$

Data presented in Figs. 5 and 6 confirm the assumption above about the general principles anent the formation of a multiband spectrum of frequencies. In the case under consideration in this section $\backslash = 3$. The eigenfrequencies of a two-level internal vibrator are defined in Eq. (26). To determine the operator that transforms the dependencies $\omega^2 = \omega^2(\boldsymbol{k})$, shown in Fig. 5, into a series of three passbands, it suffices to consider the one-dimensional oscillations of a single node (taking into account the internal microstructure) based on Eq. (15) taking into consideration external forces, as was done in deriving Eqs. (27) and (28). For the dimensionless parameters we have adopted, the corresponding equations assume the following form:

$$\begin{bmatrix} \frac{\gamma}{1+\gamma} + \Omega_e^2 - \omega^2 & -\frac{\gamma}{1+\gamma} & 0 \\ -\frac{1}{1+\gamma} & \frac{1+\beta}{1+\gamma} - \omega^2 & -\frac{\beta}{1+\gamma} \\ 0 & -\frac{\alpha\beta}{1+\gamma} & \frac{\alpha\beta}{1+\gamma} - \omega^2 \end{bmatrix} \cdot \begin{bmatrix} x_e \\ x_i \\ x_n \end{bmatrix} = 0 \tag{33}$$

The influence of the external environment is embedded in the frequency Ω_e^2. The limiting values of the frequencies, $\omega_{h,1}^2$ and $\omega_{h,2}^2$, can be found from the truncated system as represented by Eq. (34):

$$\begin{vmatrix} \frac{1+\beta}{1+\gamma}-\omega^2 & -\frac{\beta}{1+\gamma} \\ -\frac{\alpha\beta}{1+\gamma} & \frac{\alpha\beta}{1+\gamma}-\omega^2 \end{vmatrix} = 0 \tag{34}$$

Hence

$$\omega^2_{h1,2} = \frac{1+\beta+\alpha\beta \pm \sqrt{(1+\beta+\alpha\beta)^2-4\alpha\beta}}{2(1+\gamma)} \tag{35}$$

For parameters in Fig. 6, the eigenvalues are $\omega^2_{h,\,1} = 0.195$ and $\omega^2_{h,2} = 1.138$. Such estimates somewhat narrow the width of the bandgaps and expand the middle passband. The widths of these zones can be determined more accurately if we substitute in Eq. (33) the highest frequency reached in Fig. 5 (see Eq. (25)).

$$\omega^2_{M,3} \approx 1.65 \times \Omega^2 = 2.475 \tag{36}$$

The obtained values of $\omega^2_{h,\,1} = 0.156$ and $\omega^2_{h,\,2} = 1.087$ coincide with the result shown in Fig. 6(a). Data presented in Fig. 7 show the dependencies of $\omega^2_i(\boldsymbol{k})$ only along one straight line in the $\boldsymbol{k}$-space ($i = 1, 2, 3, \ldots, 18$ in the increasing order of frequencies). Graphical representation of dispersion hypersurfaces in four-dimensional space ($\boldsymbol{k},\omega$) is impossible, but it is realistic to depict the alternation of bandgaps and passbands as follows.

In a spherical coordinate system (θ, ϕ, ω^2), we define surfaces constructed by the following method. For each direction (θ,ϕ), we change the wave vector, $\boldsymbol{k}$, from $\mathbf{0}$ to the boundary of the Brillouin zone and find the extreme values as:

$$\begin{aligned} &\max_k\left[\omega^2_6(\theta,\phi;k)\right] = \omega^2_{1,h}(\theta,\phi),\ \min_k\left[\omega^2_7(\theta,\phi;k)\right] = \omega^2_{int;1}, \text{and} \\ &\max_k\left[\omega^2_{12}(\theta,\phi;k)\right] = \omega^2_{2,h}(\theta,\phi),\ \min_k\left[\omega^2_{13}(\theta,\phi;k)\right] = \omega^2_{int;2} \end{aligned} \tag{37}$$

The surfaces, $\omega^2_{(a)} = \omega^2_{1,\,h}(\theta,\phi)$ and $\omega^2_{(b)} = \omega^2_{int;\,1}$ bound the lower bandgap, and the surfaces $\omega^2_{(c)} = \omega^2_{2,\,h}(\theta,\phi)$ and $\omega^2_{(d)} = \omega^2_{int;\,2}$ bound the upper bandgap. The corresponding result for the system parameters $\alpha = 2, \beta = 1, \gamma = 2$, and $\Omega^2 = 1.5$ (as shown in Fig. 6) is presented in Fig. 9. Naturally, the passband region is bounded from below by a sphere of radius $\omega^2 = \omega^2_{int;\,1}$, and a sphere of radius $\omega^2 = \max(\omega^2_{2,\,h}) = 1.087$ from above (see Eqs. (35) and (36) and corresponding explanations).

Based on Eqs. (28) and (35), it is easy to control the passbands and bandgaps by approximating the surfaces $\omega^2_{(a)}$, $\omega^2_{(b)}$, $\omega^2_{(c)}$, $\omega^2_{(d)}$ with spheres of radii $\omega^2_{1,\,h}(\boldsymbol{k} = \mathbf{0})$, $\omega^2_{int;\,1}$, $\omega^2_{2,\,h}$, and $\omega^2_{int;\,2}$. Data represented by the surface in Fig. 10 depict the characteristic dependence of frequencies $\omega^2_{int;\,1}$ and $\omega^2_{int;\,2}$ on the parameters α and β for a fixed value of γ. It is discussed below how the upper bandgap can be adjusted based on these data (see in Fig. 6 the orange-coloured zone referred to in the sequel as the 'orange-zone').

A narrow 'orange-zone' can be formed if the frequency difference $\Delta\omega^2_{21} = 1/2(\omega^2_{int;\,2} - \omega^2_{int;\,1})$ is small relative to the frequency average value $\langle\omega^2_{21}\rangle = (\omega^2_{int;\,2} + \omega^2_{int;\,1})/2$. According to Fig. 10, one of the suitable parameter sets is: $\alpha = 7$ and $\beta = 0.5$. The corresponding result is shown in Fig. 11(a). The dependencies of frequency on the wave vector are calculated for the trajectory in $\boldsymbol{k}$-space, presented in Fig. 12. The 'orange-zone' can be significantly expanded (see Fig. 11(b)) for a large gap of $\Delta\omega^2_{21}$ ($\alpha = 0.5$ and $\beta = 0.5$ - see Fig. 10).

In Fig. 11(a) and (b), the frequency Ω^2 exceeds the value $\omega^2_{int;\,2}$. By an inverse ratio, $\Omega^2 \lesssim \omega^2_{int;\,2}$, the difference $\omega^2_{2,\,h} - \omega^2_{int;\,1}$, which is an estimation of the width of the second passband, can be significantly reduced (recall that all three hybrid frequencies depend on Ω^2 and are easily calculated based on Eq. (33)). Results in Fig. 11(c) show the possibility of forming such a rather narrow passband regions (see the olive passband) with low group velocities of acoustic waves. The results obtained for the BCC lattice are directly related to more complex 3D structures as shown in the next section.

4. The FCC-multi-resonator mass-in-mass structure

Here we demonstrate the implementation of the physical principles of bandgap formation as discussed above, using the example of an FCC substratum lattice for the MR metamaterial. We construct the mathematical description of the acoustic properties of such a system in a slightly different way than in the previous section.

When considering the BCC structure, we operated with a unit cell in the form of a cube containing two nodes. Accordingly, the entire system was presented in the form of two simple cubic sublattices. This node partitioning made it possible to map the oscillation frequency of the system, Ω^2, with wave vectors $k_x, k_y, k_z = 2\pi/a$ to the center of the Brillouin zone ($\boldsymbol{k} = \mathbf{0}$) and subsequently display hybrid frequencies at the same point ($\boldsymbol{k} = \mathbf{0}$) for interpretations and estimates of the width of bandgaps. A similar approach applied to the FCC problem (the unit cell contains 4 nodes) will force one to operate with four sublattices,

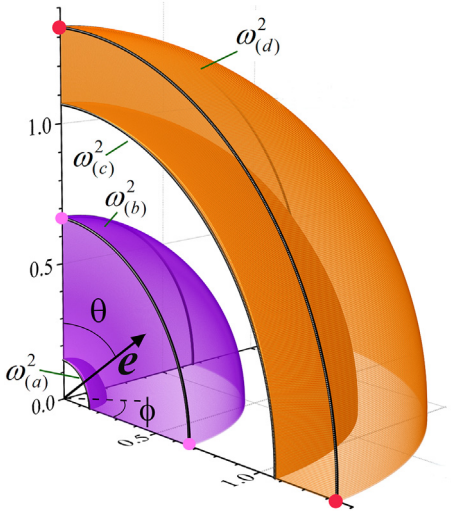

Fig. 9. Representation of bandgaps in the three-dimensional (θ, ϕ, ω^2)-space. Coordinates θ and ϕ indicate the direction along which the wave propagates ($\alpha = 2, \beta = 1, \gamma = 2$, and $\Omega^2 = 1.5$).

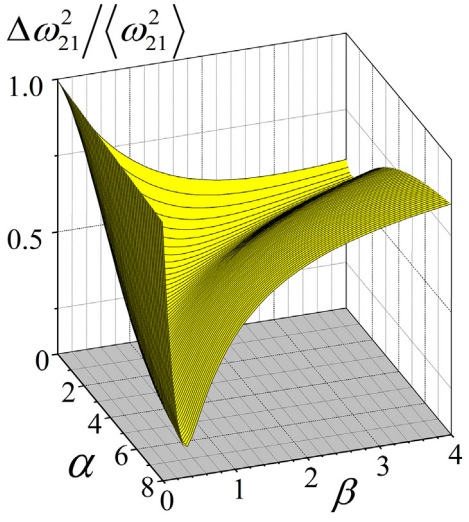

Fig. 10. The characteristic dependence of the relative amplitude of variations in eigenfrequencies of an isolated lattice site, $\Delta\omega^2_{21}/\langle\omega^2_{21}\rangle$, on parameters α and β for a fixed γ ($\gamma = 2$).

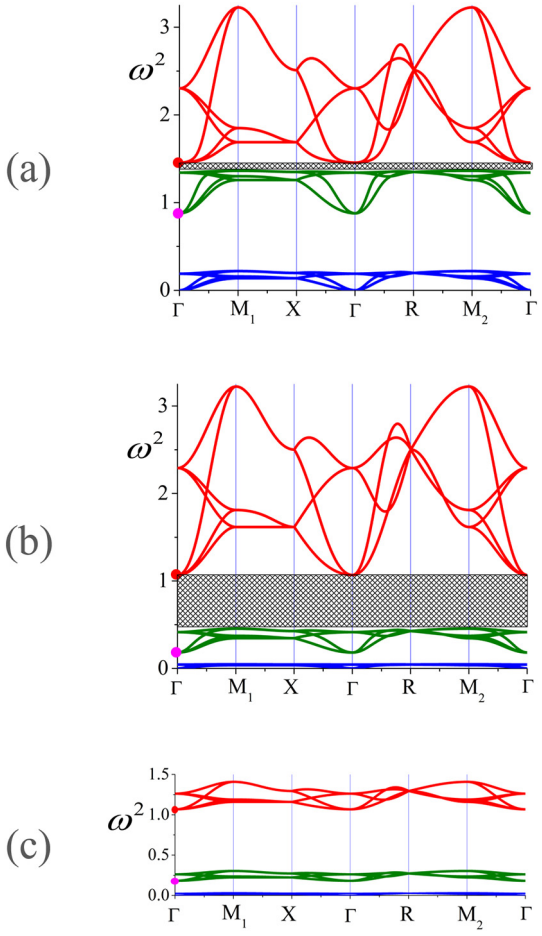

Fig. 11. Dependencies $\omega_n^2 = \omega^2(\boldsymbol{k})$ where $n = 1, 2, 3, \ldots, 18$ for different sets of system parameters. Vector $\boldsymbol{k}$ changes along the path that lies in the first octant of the Brillouin zone (see Fig. 7). (a) $\Omega^2 = 1.5$, $\alpha = 7$, $\beta = 0.5$, and $\gamma = 2$. (b) $\Omega^2 = 1.5$, $\alpha = 0.5$, $\beta = 0.5$, and $\gamma = 2$. (c) $\Omega^2 = 0.3$, $\alpha = 0.5$, $\beta = 0.5$, and $\gamma = 2$.

which greatly complicates the construction of the dispersion equation. Therefore, we operated with a primitive cell containing a single node. The corresponding translational symmetry vectors (see Fig. 13(a), red-yellow vectors) are $\ell_1\left(\frac{a}{\sqrt{2}}, \frac{a}{\sqrt{2}}, 0\right)$, $\ell_2\left(0, \frac{a}{\sqrt{2}}, \frac{a}{\sqrt{2}}\right)$, $\ell_3\left(\frac{a}{\sqrt{2}}, 0, \frac{a}{\sqrt{2}}\right)$. Each

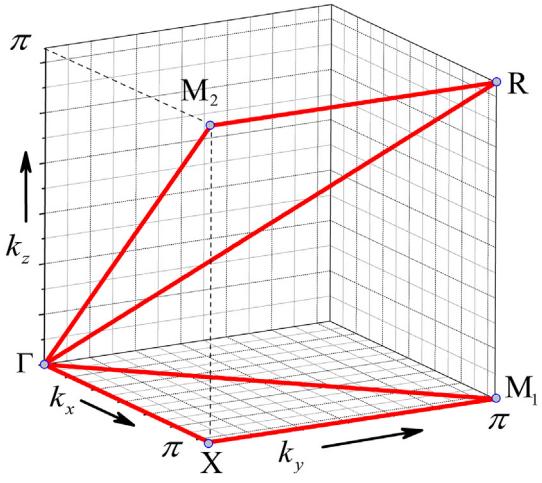

Fig. 12. The first octant of the Brillouin zone and the path along which the wave vector changes when calculating the data presented in Fig. 11.

node (marked blue) interacts with 12 nearest neighboring nodes (marked olive), placed at a distance $\frac{a}{\sqrt{2}}$ from the reference node, and six dark cyan nodes from the second-order close environment, located at a distance a (see Fig. 13(a)). The stiffness constants for the longer and shorter springs are χ and $\sqrt{2}\chi$, respectively. For the selected system of translational symmetry vectors, the first Brillouin zone in $\boldsymbol{k}$-space is a truncated octahedron as shown in Fig. 13(b) (the dimensions of the zone along the X, Y, Z axes are equal to $4\pi/a$).

When analyzing the properties of the BCC lattice, we established that in order to determine the boundaries of pass and stop bands, it is necessary to establish a set of eigenfrequencies of isolated nodes and a set of hybrid frequencies (see Eq. (32)). Both of these sets can be found from Eq. (33) for $\Omega_e^2 = 0$ and $\Omega_e^2 = \Omega_{0,\,max}^2$, respectively ($\Omega_{0,\,max}^2$ – is the highest frequency achieved in the lattice if internal multivibrators are excluded from consideration). Usually, such a frequency corresponds to a point $\boldsymbol{k}$ lying on the boundary of the Brillouin zone. These frequencies can be obtained analytically for the directions of the wave vector which coincide with the axes of symmetry of the zone.

Derived on the basis of Eqs. (3) and (4), equations of motion corresponding to the generalized coordinates of external shells of nodes x_e, y_e, z_e, (internal multivibrators have not yet been taken into account) have the form:

$$M\ddot{\boldsymbol{X}}_{ext} = \sqrt{2}\chi \boldsymbol{A}\cdot\boldsymbol{X}_{ext}, \boldsymbol{X}_{ext} = \begin{bmatrix} x_e \\ y_e \\ z_e \end{bmatrix}, \boldsymbol{X}_{ext} = \boldsymbol{X}_0 e^{i\omega t}$$
$$\rightarrow \left|\frac{\sqrt{2}\chi}{M}\boldsymbol{A} + \omega^2\right|\cdot\boldsymbol{X}_0 = 0 \tag{38}$$

where

$$A_{11} = a_{xy} + a_{xz} - 4 + \sqrt{2}(\cos k_x - 1)$$
$$A_{22} = a_{xy} + a_{yz} - 4 + \sqrt{2}(\cos k_y - 1)$$
$$A_{33} = a_{xz} + a_{yz} - 4 + \sqrt{2}(\cos k_z - 1)$$

$$a_{xy} = 2\cos(k_x/2)\cos(k_y/2), a_{xz} = 2\cos(k_x/2)\cos(k_z/2), a_{yz} = 2\cos(k_y/2)\cos(k_z/2)$$

$$A_{12} = A_{21} = -2\sin(k_x/2)\sin(k_y/2), A_{13} = A_{31} = -2\sin(k_x/2)\sin(k_z/2), \text{ and } A_{23} = A_{32} = -2\sin(k_y/2)\sin(k_z/2)$$

The highest eigenfrequencies of the lattice calculated for the boundary points of the Brillouin zone $X(2\pi,0,0)$, $K(3\pi/2,3\pi/2,0)$, $\Sigma(\pi,\pi,0)$ and $L(\pi,\pi,\pi)$ (see Fig. 15(b)) are equal, respectively, to:

$$\omega_X^2 = \frac{\chi}{M}8\sqrt{2}, \omega_K^2 = \frac{\chi}{M}4\left(1+\sqrt{2}\right), \omega_\Sigma^2 = \frac{\chi}{M}\left(6\sqrt{2}+4\right), \text{and } \omega_L^2 = \frac{\chi}{M}\left(8\sqrt{2}+4\right) \tag{39}$$

These frequencies are indicated by circles in Fig. 14(a). The highest frequency is achieved for the dimensionless wave vector $\boldsymbol{k}(\pi,\pi,\pi)$ and corresponds to the longitudinal vibrations of the [111]-layers of the lattice nodes with a wavelength of $\lambda = \frac{2}{3}\left(a\sqrt{3}\right)$ which means that neighboring [111] layers, spaced apart by $a/\sqrt{3}$ distance, oscillate in antiphase.

In the presence of internal multivibrators, the formation of bandgaps and passbands in between them obeys the same laws as in the case of the BCC lattice. The equation of motion for the coordinates of the elements of the system below.

$$\boldsymbol{X} = \begin{bmatrix} \boldsymbol{X}_{ext} \\ \boldsymbol{X}_{int} \\ \boldsymbol{X}_{nuc} \end{bmatrix}, \boldsymbol{X}_{int} = \begin{bmatrix} x_i \\ y_i \\ z_i \end{bmatrix}, \boldsymbol{X}_{nuc} = \begin{bmatrix} x_n \\ y_n \\ z_n \end{bmatrix} \tag{40}$$

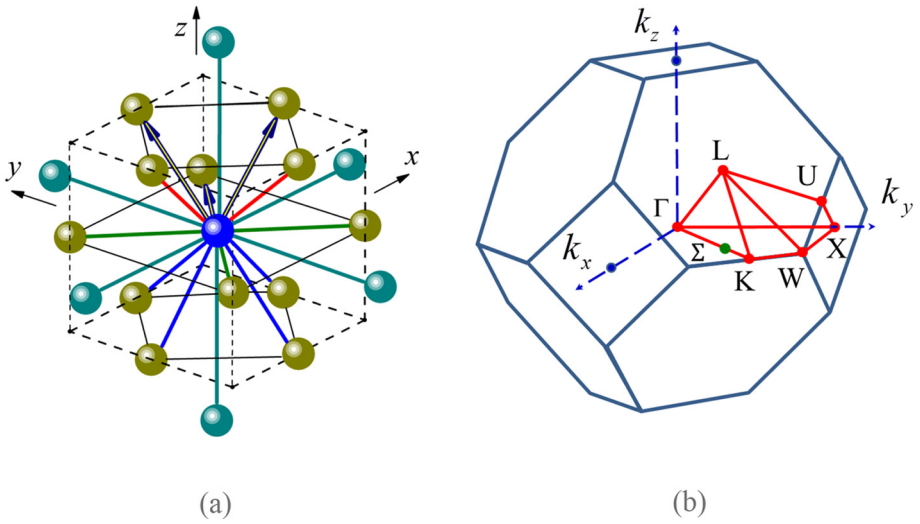

Fig. 13. (a) The FCC lattice: the interaction scheme of the referenced lattice node (blue) with the nearest nodes (olive) and second-order nearest nodes (dark cyan). (b) The first Brillouin zone for the FCC lattice. (For interpretation of the references to colour in this figure legend, the reader is referred to the web version of this article.)

have the form:

$$\begin{bmatrix} M\cdot\ddot{\boldsymbol{X}}_{ext} \\ m_i\cdot\ddot{\boldsymbol{X}}_{int} \\ m_n\cdot\boldsymbol{X}_{nuc} \end{bmatrix} = \begin{bmatrix} \sqrt{2}\chi\cdot\boldsymbol{A}-2\kappa_i\cdot\boldsymbol{I}_3 & 2\kappa_i\cdot\boldsymbol{I}_3 & 0 \\ 2\kappa_i\cdot\boldsymbol{I}_3 & -(2\kappa_i+2\kappa_n)\cdot\boldsymbol{I}_3 & 2\kappa_n\cdot\boldsymbol{I}_3 \\ 0 & 2\kappa_n\cdot\boldsymbol{I}_3 & -2\kappa_n\cdot\boldsymbol{I}_3 \end{bmatrix}\cdot\begin{bmatrix} \boldsymbol{X}_{ext} \\ \boldsymbol{X}_{int} \\ \boldsymbol{X}_{nuc} \end{bmatrix}$$

from which the equation for determining the eigenfrequencies and eigenvectors, $\boldsymbol{X}_0$ follows:

$$-\omega^2\boldsymbol{X}_0 = \begin{bmatrix} \Omega^2\cdot\eta\boldsymbol{A}-\dfrac{\gamma}{1+\gamma}\cdot\boldsymbol{I}_3 & \dfrac{\gamma}{1+\gamma}\cdot\boldsymbol{I}_3 & \boldsymbol{0} \\ \dfrac{1}{1+\gamma}\cdot\boldsymbol{I}_3 & -\dfrac{\gamma+\beta}{1+\gamma}\cdot\boldsymbol{I}_3 & \dfrac{\beta}{1+\gamma}\cdot\boldsymbol{I}_3 \\ \boldsymbol{0} & \dfrac{\alpha\beta}{1+\gamma}\cdot\boldsymbol{I}_3 & -\dfrac{\alpha\beta}{1+\gamma}\cdot\boldsymbol{I}_3 \end{bmatrix}\cdot\boldsymbol{X}_0 \qquad (41)$$

Here $\eta=\frac{1}{8+2\sqrt{2}}$, and parameters, α, β,and γ are defined, as before, by Eq. (24). The fourth parameter is the dimensionless eigenvalue defined by the ratio $\Omega^2=\omega_L^2/\omega_0^2$ (the definition of ω_0^2 is given in Eq. (18)).

In Fig. 14(a) the frequency characteristics of the system are depicted along the path ΓXWKΓLKWLUX in the $\boldsymbol{k}$-space (see Fig. 13(b)). The results obtained from Eq. (38) when internal multivibrators are not taken into account and for the value of the parameter $\Omega^2=1.5$ are shown in Fig. 14(a). The effect of turning the multivibrators on is shown in Fig. 14(b) with conspicuous gaps in between dispersion curves (projections of dispersion surfaces). It can be seen that the topology of the dependences $\omega^2(\boldsymbol{k})$ in the three passbands is an analog of the topology of the set of dependencies obtained in the "initial state" - see Fig. 14(a).

We should emphasize that the upper boundaries of the bandgaps, $\omega^2=\omega^2_{int,\,1}=2/3$ and $\omega^2=\omega^2_{int,\,2}=4/3$, as well as their lower boundaries, $\omega^2=\omega^2_{h,\,1}=0.137$ and $\omega^2=\omega^2_{h,\,2}=1.05$ can be precisely determined in advance by Eq.(33) by substituting $\Omega_e^2=0$ and $\Omega_e^2=\Omega^2$, respectively, without solving Eq.(41). The value $\omega^2_{h,\,3}\approx 2.31$ defines the upper bound of all possible wave frequencies that can propagate in the system.

The revealed patterns of formation of passbands are applicable for more complex multivibrators (see Fig. 15). Here we present the result

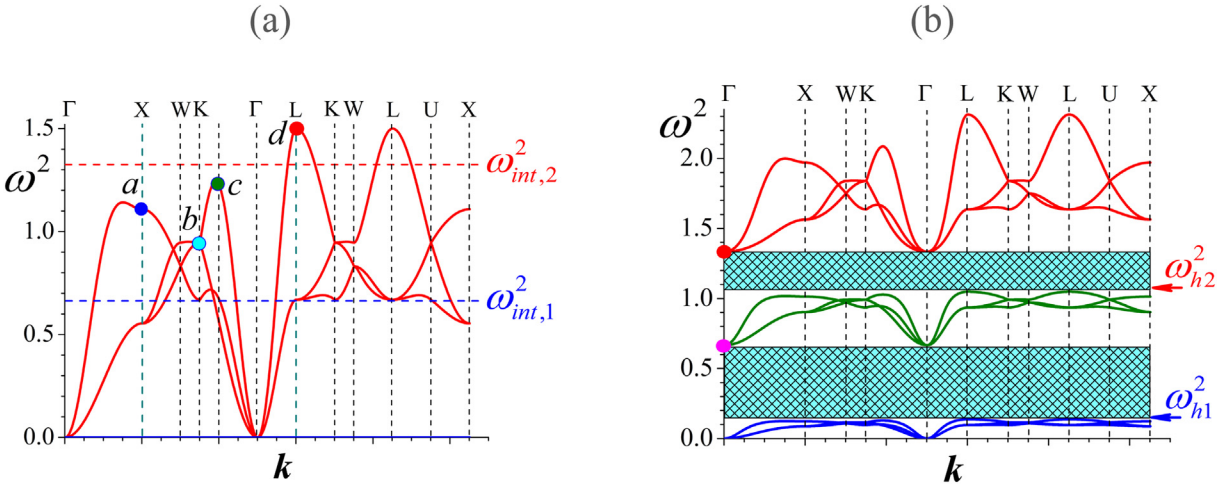

Fig. 14. (a) The initial set of dependences $\omega^2(\boldsymbol{k})$ along a trajectory in the $\boldsymbol{k}$-space. $\Omega^2=1.5$. (b) The manifestation factor of a three-level multivibrator ($\alpha=2$, $\beta=1$,and $\gamma=2$).

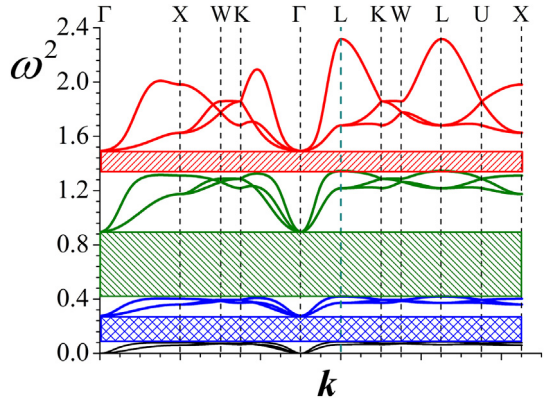

Fig. 15. The manifestation of an additional core inside the lattice node for the system shown in Fig. 14 ($\Omega^2 = 1.5, \alpha = 2, \beta = 1, \gamma = 2, \alpha' = 2$, and $\beta' = 0.5$).

for the case when three internal masses are located inside the node: the central core of mass m_c is added to the masses m_i and m_n. The stiffness of the springs that connect this core with the adjacent shell is k_c. Therefore, to the four previously used parameters $\alpha, \beta, \gamma, \Omega^2$, two more dimensionless parameters should be added - $\alpha' = m_a/m_c, \beta' = k_c/k_a$.

Data presented in Fig. 15 is quite expected. Four passbands reproduce the structure of dependencies, shown in Fig. 14 (a), in different frequency ranges. The upper/lower boundaries of the bandgaps, $\Delta^2_{sup,i}$ $(i = 1, 2, 3)$, displayed in Fig. 15, exactly correspond to the eigenfrequencies of the equation presented below for $\Omega_e^2 = 0$ and $\Omega_e^2 = \Omega^2$.

$$\begin{bmatrix} \frac{\gamma}{1+\gamma}+\Omega_e^2-\omega^2 & -\frac{\gamma}{1+\gamma} & 0 & 0 \\ -\frac{1}{1+\gamma} & \frac{1+\beta}{1+\gamma}-\omega^2 & -\frac{\beta}{1+\gamma} & 0 \\ 0 & -\frac{\alpha\beta}{1+\gamma} & \frac{\alpha(\beta+\beta')}{1+\gamma}-\omega^2, & -\frac{\alpha\beta'}{1+\gamma} \\ 0 & 0 & -\frac{\alpha\beta'}{1+\gamma} & \frac{\alpha\beta'}{1+\gamma} \end{bmatrix} \cdot \begin{bmatrix} x_e \\ x_i \\ x_n \\ x_c \end{bmatrix} = 0 \tag{42}$$

This equation is an extension of Eq. (31), which takes into account the additional vibrator/internal mass. Its solutions are $\omega^2_{int,1}$=0.277, $\omega^2_{int,2}$=0.896, $\omega^2_{int,\ 3}$=1.493 ($\Omega_e^2 = 0$) and $\omega^2_{h,1}$=0.085, $\omega^2_{h,2}$=0.420, $\omega^2_{h,3}$=1.344 ($\Omega_e^2 = \Omega^2$). The value $\omega^2_{h,\ 4}$=2.317 determines the highest frequency in the upper passband. The widths of the bandgaps are given, in accordance with Eq. (32), as $\Delta^{(\omega^2)}_{sup,i} = \omega^2_{int,i} - \omega^2_{h,i}$, $i = 1, 2, 3$.

5. Conclusions

The present study deals with the extraction of dispersion surfaces, passbands, and bad gaps for 3D discrete parameter multi-resonator phononic metamaterials. The investigation has considered the simple case of locally isotropic homogeneous model where all nodes have the same internal microstructure comprising nodal point masses connected by springs of equal stiffness in three mutually perpendicular directions. The main result of the conducted study is the established laws for creating a multiband acoustic system based on the multilevel internal microstructure within the lattice nodes. We have shown that the solution to such a problem splits into two stages.

In the first stage, only the desired "initial" structure of dispersion surfaces $\omega_n^2(\boldsymbol{k})$ of the acoustic system is formed by choosing the type of symmetry of the lattice nodes (internal multivibrators are excluded from consideration, $n = 1, 2, 3, \ldots, N$, where N is the number of degrees of freedom). The topology of this set of surfaces does not depend on the ratio χ/M (where χ is the stiffness of external springs, and M is the mass of nodes (mass of external shells)). A general parameter of the initial set $\omega_n^2(\boldsymbol{k})$ is its upper boundary Ω_e^2, which can usually be found analytically from the dispersion equation for the initial structure. In the second stage, only the relations between the parameters of the internal microstructure of the nodes (multivibrators) are optimized to form the relations between the required boundary frequencies of the passbands or bandgaps. These frequencies can be found from easily constructed dispersion equations of the n-th order e.g. second-, third-, or fourth-order (depending on the number of levels in the internal structure of the nodes). All these boundary frequencies are shifted to the desired range of real frequencies by the parameter Ω_e^2 (which is proportional to the value of χ). Herewith, each passband is an exact topological copy of the original set $\omega_n^2(\boldsymbol{k})$.

The value of the parameter Ω_e^2 may be chosen to be either above the maximum natural frequency of the isolated lattice node, $\omega^2_{int;max}$, or below it. In the latter case, a passband is generated in the range $\omega^2_{n,hibr}(\boldsymbol{k}) > \omega^2_{int;\ max}$. The variation of the gap $\Omega_e^2 - \omega^2_{int;max}$ changes the width of the passbands, determining different group velocities of acoustic waves in each of them.

It is thus concluded that the use of multivibrators in acoustic metamaterials makes it possible to form the desired properties of elastic media on the basis of our simple method for predicting these properties depending on the controlled parameters of the multivibrators and the environment external to them. This depends on the topology as well as the geometric properties of the external medium. Controlled formation of pass and stop bands, in terms of number and size may be achievable through alteration of model parameters defining the MR metastructure uniquely.

Note that our work concerns the development of concepts on the mechanism of bandgap formation in acoustic metamaterials based on an ordered lattice of multivibrators. Such a problem was previously considered for a one-dimensional chain of multivibrators [7,32]. The possibility of the formation of bandgaps is analyzed in terms of the effective mass of lattice sites (gaps correspond to negative effective mass). This method leads to the analysis of the properties of a multiparameter mathematical expression, which complicates the choice of optimal parameters for the entire system in 3D cases with a complex morphology of the internal structure of the lattice nodes. In our method, through dividing the problem into the two stages described above, the task of searching for the required optimum is greatly simplified. Taking into account dissipation processes in real structures (in a one-dimensional case this was done in [20]) will not introduce additional problems when using the method presented in our work, since the guaranteed bandgap boundaries are determined with the eigenfrequencies of isolated multivibrators and multivibrators with fixed outer shells (these frequencies will be merely shifted if the dissipative factors are taken into account).

A final remark is in order here. While microstructure continuum modelling of such MR metamaterials is possible, similar to the works done on SR metamaterials [33,34], this has not been found to provide specifically more information on the dispersion surface topology nor on the band structure of the MR metamaterial. Furthermore, advanced numerical techniques need to be used to solve the homogenised continuum models' equations relating to phenomena such as quantum level repulsion, energy splitting, strong coupling, and level crossings [35–37]. In order to achieve additional flexibility, more intricate designs might be needed to render possible additional features as directional dependence of wave propagation [6], anisotropy in waveguides [2,14], or traction-direction dependence in filtering [10,14].

Data availability

The raw/processed data required to reproduce these findings cannot be shared at this time as the data also forms part of an ongoing study.

Author statement

Vyacheslav N. Gorshkov: Conceptualization, Formal analysis, Supervision, Writing-original draft, Writing-review and editing. Pooya Sareh: Investigation, Visualization, writing-original draft. Navid Navadeh: Methodology, Visualization. Vladimir V. Tereshchuk: Investigation, Software. Arash S. Fallah: Conceptualization, Investigation, Project administration, Supervision, Writing-original draft, Writing-review and editing.

Declaration of Competing Interest

The authors declare that they have no known competing financial interests or personal relationships that could have appeared to influence the work reported in this paper.

References

[1] H.H. Huang, C.T. Sun, G.L. Huang, On the negative effective mass density in acoustic metamaterials, Int. J. Eng. Sci. 47 (4) (2009) 610–617.
[2] V.N. Gorshkov, N. Navadeh, A.S. Fallah, A study of frequency band structure in two-dimensional homogeneous anisotropic phononic K-3-metamaterials, Smart Mater. Struct. 26 (2017) 9.
[3] Y.Y. Chen, et al., Dissipative elastic metamaterials for broadband wave mitigation at subwavelength scale, Compos. Struct. 136 (2016) 358–371.
[4] S. Krodel, N. Thome, C. Daraio, Wide band-gap seismic metastructures, Extreme Mech. Lett. 4 (2015) 111–117.
[5] Y.Y. Chen, et al., Enhanced flexural wave sensing by adaptive gradient-index metamaterials, Sci. Rep. (2016) 6.
[6] M. Maldovan, Sound and heat revolutions in phononics, Nature 503 (7475) (2013) 209–217.
[7] G.L. Huang, C.T. Sun, Band gaps in a multiresonator acoustic metamaterial, J. Vibr. Acoustics Trans. Asme 132 (2010) 3.
[8] H.W. Dong, et al., Robust 2D/3D multi-polar acoustic metamaterials with broadband double negativity, J. Mech. Phys. Solids 137 (2020).
[9] B.S. Lazarov, J.S. Jensen, Low-frequency band gaps in chains with attached nonlinear oscillators, Int. J. Non-Linear Mech. 42 (10) (2007) 1186–1193.
[10] A.S. Fallah, et al., Phononic dispersion in anisotropic pseudo-fractal hyper-lattices, Mater. Des. 164 (2019).
[11] A.O. Krushynska, F. Bosia, N.M. Pugno, Labyrinthine acoustic metamaterials with space-coiling channels for low-frequency sound control, Acta Acust. United Acust. 104 (2) (2018) 200–210.
[12] X.F. Man, et al., Hilbert fractal acoustic metamaterials with negative mass density and bulk modulus on subwavelength scale, Mater. Des. (2019) 180.
[13] K.T. Tan, H.H. Huang, C.T. Sun, Optimizing the band gap of effective mass negativity in acoustic metamaterials, Appl. Phys. Lett. 101 (2012) 24.
[14] A.S. Fallah, et al., Wave propagation in two-dimensional anisotropic acoustic metamaterials of K4 topology, Wave Motion 58 (2015) 101–116.
[15] J. Li, C.T. Chan, Double-negative acoustic metamaterial, Phys. Rev. E 70 (2004) 5.
[16] V.N. Gorshkov, et al., Sonic metamaterials: reflection on the role of topology on dispersion surface morphology, Mater. Des. 132 (2017) 44–56.
[17] S.A. Cummer, J. Christensen, A. Alu, Controlling sound with acoustic metamaterials, Nat. Rev. Mater. 1 (2016) 3.
[18] S.H. Lee, et al., Acoustic metamaterial with negative density, Phys. Lett. A 373 (48) (2009) 4464–4469.
[19] M.V. Barnhart, et al., Experimental demonstration of a dissipative multi-resonator metamaterial for broadband elastic wave attenuation, J. Sound Vib. 438 (2019) 1–12.
[20] Q.Q. Li, Z.C. He, E. Li, Dissipative multi-resonator acoustic metamaterials for impact force mitigation and collision energy absorption, Acta Mech. 230 (8) (2019) 2905–2935.
[21] Y. Wu, M. Yang, P. Sheng, Perspective: acoustic metamaterials in transition, J. Appl. Phys. 123 (2018) 9.
[22] L. Bonanomi, G. Theocharis, C. Daraio, Wave propagation in granular chains with local resonances, Phys. Rev. E 91 (2015) 3.
[23] B.W. Li, ACOUSTICS now you hear me, now you don't, Nat. Mater. 9 (12) (2010) 962–963.
[24] X.F. Li, et al., Tunable unidirectional sound propagation through a sonic-crystal-based acoustic diode, Phys. Rev. Lett. 106 (2011) 8.
[25] R. Martinezsala, et al., Sound-attenuation by sculpture, Nature 378 (6554) (1995) 241.
[26] T. Gorishnyy, et al., Hypersonic phononic crystals, Phys. Rev. Lett. 94 (2005) 11.
[27] Z.Y. Liu, et al., Locally resonant sonic materials, Science 289 (5485) (2000) 1734–1736.
[28] P. Sheng, et al., Dynamic mass density and acoustic metamaterials, Physica B-Condensed Matter 394 (2) (2007) 256–261.
[29] X.L. Wang, et al., Acoustic perfect absorption and broadband insulation achieved by double-zero metamaterials, Appl. Phys. Lett. 112 (2018) 2.
[30] G.C. Ma, P. Sheng, Acoustic metamaterials: from local resonances to broad horizons, Sci. Adv. 2 (2016) 2.
[31] J.T. Liu, et al., Tunable ultra-narrow band-gap of anomalous dispersion photonic crystals, Epl 78 (2007) 5.
[32] Q.Q. Li, et al., Design of a multi-resonator metamaterial for mitigating impact force, J. Appl. Phys. 125 (2019) 3.
[33] R. Zhu, et al., Microstructure continuum modeling of an elastic metamaterial, Int. J. Eng. Sci. 49 (12) (2011) 1477–1485.
[34] A.P. Liu, et al., Multi-displacement microstructure continuum modeling of anisotropic elastic metamaterials, Wave Motion 49 (3) (2012) 411–426.
[35] O. Rokos, et al., Micromorphic computational homogenization for mechanical metamaterials with patterning fluctuation fields, J. Mech. Phys. Solids 123 (2019) 119–137.
[36] A. Sridhar, V.G. Kouznetsova, M.G.D. Geers, A general multiscale framework for the emergent effective elastodynamics of metamaterials, J. Mech. Phys. Solids 111 (2018) 414–433.
[37] A. Sridhar, et al., Homogenized enriched continuum analysis of acoustic metamaterials with negative stiffness and double negative effects, J. Mech. Phys. Solids 119 (2018) 104–117.